photonics

MDPI

Article

Incandescent Light Bulbs Based on a Refractory Metasurface †

Hirofumi Toyoda [1], Kazunari Kimino [1], Akihiro Kawano [1] and Junichi Takahara [1,2,*]

[1] Graduate School of Engineering, Osaka University, Osaka 565-0871, Japan; toyoda@ap.eng.osaka-u.ac.jp (H.T.); kimino@ap.eng.osaka-u.ac.jp (K.K.); a.kawano@ap.eng.osaka-u.ac.jp (A.K.)

[2] Photonics Center, Graduate School of Engineering, Osaka University, Osaka 565-0871, Japan

* Correspondence: takahara@ap.eng.osaka-u.ac.jp; Tel.: +81-6-6879-8503

† Invited paper.

Received: 5 September 2019; Accepted: 9 October 2019; Published: 12 October 2019

Abstract: A thermal radiation light source, such as an incandescent light bulb, is considered a legacy light source with low luminous efficacy. However, it is an ideal energy source converting light with high efficiency from electric power to radiative power. In this work, we evaluate a thermal radiation light source and propose a new type of filament using a refractory metasurface to fabricate an efficient light bulb. We demonstrate visible-light spectral control using a refractory metasurface made of tantalum with an optical microcavity inserted into an incandescent light bulb. We use a nanoimprint method to fabricate the filament that is suitable for mass production. A 1.8 times enhancement of thermal radiation intensity is observed from the microcavity filament compared to the flat filament. Then, we demonstrate the thermal radiation control of the metasurface using a refractory plasmonic cavity made of hafnium nitride. A single narrow resonant peak is observed at the designed wavelength as well as the suppression of thermal radiation in wide mid-IR range under the condition of constant surface temperature.

Keywords: incandescent light bulb; thermal radiation; refractory metal; microcavity; metamaterial; metasurface; surface plasmon; infrared emitter; nanoimprint

1. Introduction

An incandescent filament shining in a transparent glass bulb is the origin of the beauty of lighting. The presence of incandescent light can stimulate a brilliant human mind and exert a calming effect. In addition, incandescent light displays a continuous spectrum of thermal radiation that is attractive from the point of view of architecture, lighting design, and print color-matching. However, a thermal radiation light source like an incandescent light bulb is a legacy light source, and in recent years, its applications have decreased. This is because the luminous efficacy of an incandescent light bulb is only 15 lm·W^{-1}, which is much lower than the emerging solid-state light sources, viz., the light-emitting diode (LED) light bulbs. Most of the radiative power emitted from an incandescent light bulb is in infrared (IR) light. Hence the luminous efficacy of an incandescent light bulb is low compared to an LED light bulb because the luminous efficacy is limited to the narrow absorption band of the human eye. Additionally, the lifetime of LED light bulbs is 40,000–50,000 h which is much longer than that of incandescent light bulbs (1000–2000 h).

In contradiction to the trend favoring the use of LEDs over incandescent light bulbs, we propose that a thermal radiation light source is an ideal, high-efficiency converter of electric input power to a radiative output power source. The energy conversion efficiency of incandescent light bulbs is higher than 90%, which is a result of the Joule heating of a filament [1,2]. Hence thermal radiation light

sources have great potential for use as efficient light sources. Although the thermal radiation spectrum obeys Planck's law that depends on physical constants and temperature, its luminous efficacy can be improved beyond that suggested by Planck's law, if the thermal radiation spectra from a filament can be controlled artificially and optimized to the absorption band of human eyes.

The basic concept for improving the efficiency of an incandescent light bulb by thermal radiation control of a nanostructured filament was proposed by Waymouth in 1989 [3,4]. He reasoned that IR radiation (longer wavelengths) can be suppressed by the cut-off effect of a microcavity while visible light (shorter wavelengths) is radiated into free-space, which is analogous to the operation of a microwave waveguide. This idea is known as the Waymouth hypothesis, and the lamp is called a "microcavity lamp." Figure 1 shows the concept of the microcavity lamp, where a cuboidal hole array is formed on the surface of a tungsten (W) filament set into a bulb. Following the viewpoint of modern photonics, such an artificial surface structure is called a "metasurface," i.e., a two-dimensional (2D) metamaterial.

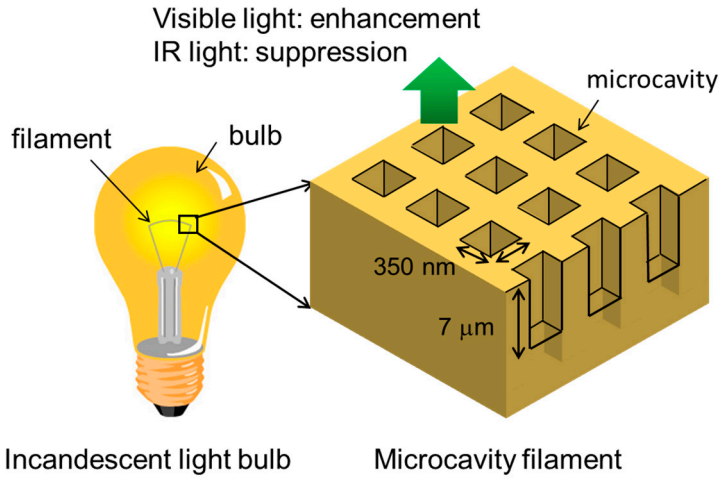

Figure 1. The concept of a microcavity lamp: an incandescent light bulb with a microcavity array filament acting as a refractory metasurface.

Independent of the Waymouth hypothesis, the modification of a thermal radiation spectrum (deviation from Planck's law) using a microstructured surface was demonstrated first in 1986 by a deep silicon grating [5]. This was studied further using various types of micro and nanostructures such as an open-end metallic microcavity [6,7], photonic crystal [8,9], plasmonic cavity [10,11], and Mie resonators [12]. Additionally, narrow-band thermal radiation has been reported using surface waves such as surface phonon polaritons [13], surface plasmon polaritons [14,15], spoof surface plasmons [16], and Tamm plasmons [17]. In 2008, perfect absorbers based on metamaterials were proposed [18,19]. In addition, thermal radiation emitters based on metasurfaces using metal-dielectric-metal (MDM) structures were demonstrated in the infrared (IR) range [20,21]. In the last decade, much research was done on perfect absorbers based on MDM metasurfaces, and their applications such as thermal radiation emitters or gas sensing in the IR range [22–29]. There are many papers about thermal radiation control based on metasurfaces in the IR range. A comprehensive list of these efforts can be found in the literature [30,31].

In contrast to the IR range, there are a few studies about thermal radiation control in the visible spectrum. This occurs because the melting points of typical plasmonic materials such as gold (Au) and silver (Ag) are below 1500 K. Additionally, damage during the nanofabrication process induces a decrease in the melting points of refractory metals due to defects. This reduces the durability of nanostructures compared with bulk materials. It was reported that Tungsten microcavity structures degrade the melting point to just above 1500 K, which was then held at 1400 K, less than one-half its melting point [32]. In 2015, we fabricated a microcavity lamp utilizing nanoimprint technology and

demonstrated the enhancement of visible light using a microcavity filament [33,34]. In 2016, Ilic et al. reported an efficient thermal light source that radiated only visible light (cut IR light emission from the filament) by directly sandwiching a dielectric multilayer filter [35]. However, it is still challenging to construct an efficient incandescent light bulb with a filament controlled by a refractory metasurface.

In this paper, we review our recent work on thermal radiation control for incandescent light bulbs based-on refractory metasurfaces. First, we demonstrate the spectral control of visible light using an optical microcavity array fabricated on a filament inserted in a light bulb. Here, a nanoimprint method is used to mass-produce the filaments. Then, to overcome the drawback of a microcavity, we introduce a refractory metasurface based on a plasmonic cavity made from hafnium nitride (HfN), which is a new kind of refractory plasmonic material. We demonstrate spectral control in the mid IR range using this new refractory metasurface.

2. The Efficiency of Thermal Radiation Light Sources

Figure 2 shows the power flow for typical commercial light sources: an incandescent light bulb with and without inert gases (inert gases were not used in old incandescent lamps), a fluorescent lamp, and an LED light bulb [1,2]. In Figure 2, we show the ratio (percentage) of output power to input electric power. Here, all power flow data are taken from [36–40].

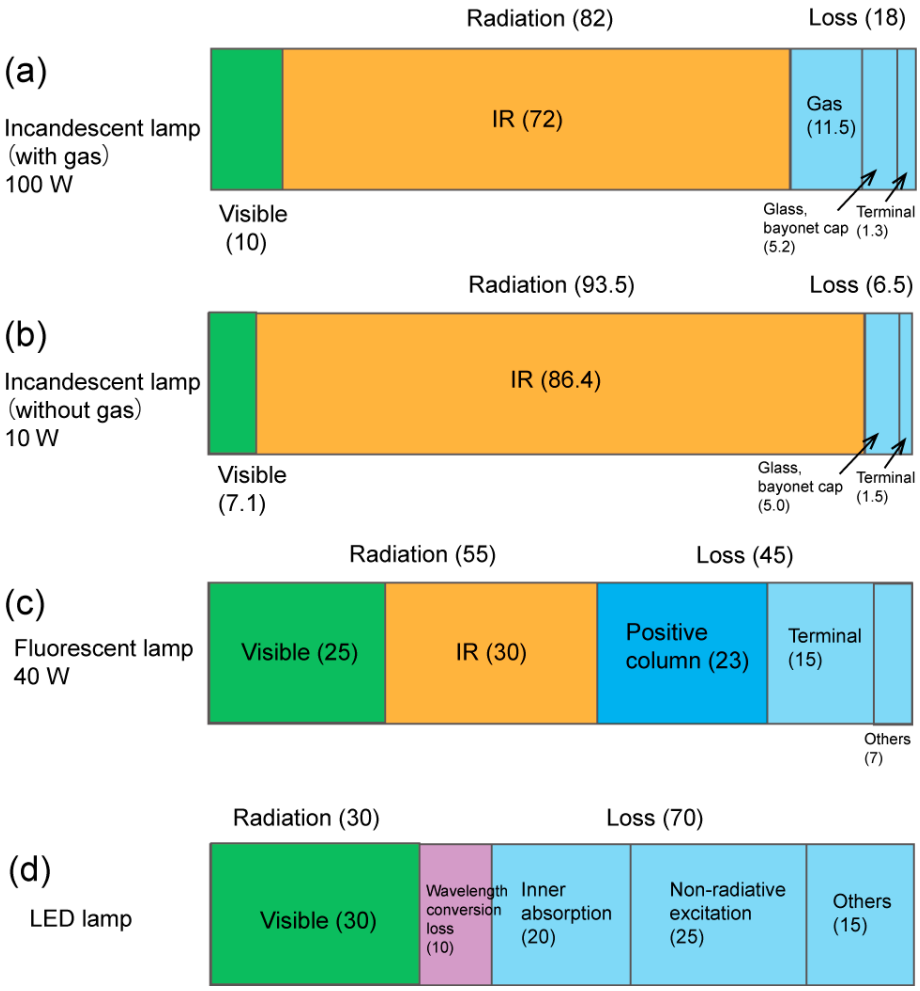

Figure 2. The power flow ratio (percentage) of typical commercial light sources: (**a**) an incandescent light bulb with inert gases (100 W) [36,37], (**b**) an incandescent light bulb without inert gases (10W) [38], (**c**) a fluorescent lamp (40 W) [39], and (**d**) a light-emitting diode (LED) light bulb (blue LED + yellow phosphor) [40].

For an LED light bulb, the conversion ratio from input power to visible light is 30–50% while it is only 10% for an incandescent light bulb with inert gas. The LED light bulb is more efficient than the incandescent light bulb. The energy loss of an LED light bulb is caused by various physical processes such as wavelength-conversion losses, inner absorption, or non-radiative phonon excitation, resulting in the dissipation of energy to the environment around the bulb. However, considering the conversion ratio from input power to total electromagnetic radiation, it is higher than 80% for the incandescent light bulb. Additionally, it exceeds 90% (~94%) for an incandescent light bulb without inert gas. This latter result is obtained because the loss of heat conduction from the filament to inert gas is negligible. Thus, we can conclude that a thermal radiation light source is an ideal high-efficiency energy converter from input electric power to output radiative power. If we suppress the IR light and convert it to visible light, incandescent light bulbs can be recreated as an efficient light source.

3. The Basic Principle of Thermal Radiation Control by a Refractory Metasurface

There are two ways to suppress IR light from incandescent lamps: (i) use of an optical filter coated on a bulb and (ii) thermal radiation control of a filament. For optical filters, dielectric multilayers are used for short-pass (IR rejection) optical filters. Although short-pass optical filters are used for commercially available halogen light bulbs, the shapes of blubs are limited to elliptical, and the transparency of the bulb is reduced due to coloring of the dielectric multilayers, resulting in a reduction of the beauty of incandescent light bulbs. In contrast, using thermal radiation control, we can modify the thermal radiation spectrum for a filament directly by forming nanostructures on it. In this method, IR light is suppressed, and visible light is enhanced from a filament directly, resulting in a significant improvement in the luminous efficacy.

Spectral radiant intensity $I_{\mathrm{bb}}(\lambda,T)$ [$\mathrm{W{\cdot}m^{-2}{\cdot}m^{-1}{\cdot}sr^{-1}}$] of blackbody radiation per area and per solid angle at temperature T and wavelength λ is given by Equation (1):

$$I_{bb}(\lambda, T) = \frac{2hc^2}{\lambda^5} \frac{1}{e^{hc/\lambda k_B T} - 1}, \tag{1}$$

where c is the speed of light, h is the Planck constant, and k_{B} is the Boltzmann constant. The thermal radiation spectrum from a real surface can be calculated by the product of $I_{\mathrm{bb}}(\lambda,T)$ and spectral emissivity $\varepsilon(\lambda)$. Hence, we can control the radiation spectrum artificially by specifying $\varepsilon(\lambda)$. This is the basic principle of thermal radiation control.

In a microcavity lamp, $\varepsilon(\lambda)$ can be controlled by a microcavity array formed on the surface of a refractory metal filament. Figure 3a shows a schematic view of a cuboidal hole microcavity array. Such a cuboidal hole behaves as an open-end cavity for optical electromagnetic (EM) fields, and they are confined inside the hole. Contrary to the Waymouth hypothesis, previous experimental studies in the IR range demonstrated that a microcavity enhances thermal radiation at specific wavelengths by resonance instead of suppression by the cut-off effect [6,7]. The resonant wavelength of the microcavity (Figure 3a) is given by Equation (2):

$$\lambda = \frac{2}{\sqrt{\left(\frac{n_x}{a}\right)^2 + \left(\frac{n_y}{a}\right)^2 + \left(\frac{n_z}{2d}\right)^2}}, \tag{2}$$

where n_{x}, n_{y} = 0, 1, 2, 3 … are mode numbers of the x- or y- (horizontal) direction, respectively, and n_{z} = 0, 1, 3, 5 … is the mode number of the z- (vertical) direction, a and d are the width in the x-y direction and the depth of the cuboidal cavity, respectively [5,6].

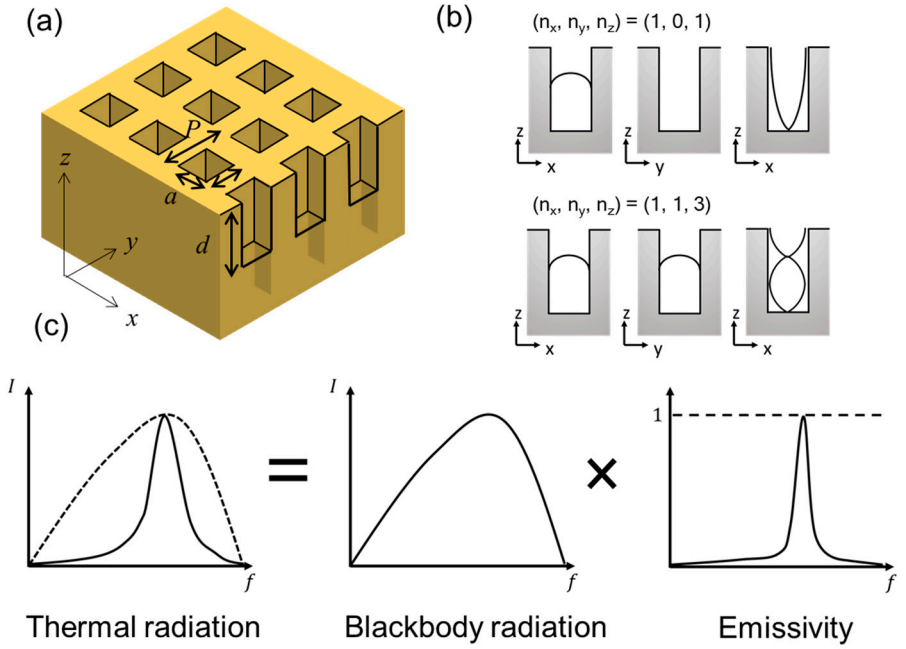

Figure 3. Principle of thermal radiation control by a metasurface: (**a**) an array of a microcavity on a refractory metal filament, (**b**) resonant modes for n = 1, 3, and 5 inside a microcavity with perfect conductor walls, and (**c**) the thermal radiation spectrum can be controlled by the product of spectral emissivity of the metasurface and Planck's law.

Figure 3b shows typical resonant modes in the cavity. In principle, such resonant modes can enhance absorption at the resonant wavelengths. According to Kirchhoff's law, such resonant absorption increases the emissivity of opaque materials in thermal radiation. On a metallic surface, emissivity is very low at non-resonant wavelengths, as shown in Figure 3c, resulting in a steep resonant enhancement of the spectral emissivity $\varepsilon(\lambda)$. Hence, the total radiation spectrum can be controlled by $\varepsilon(\lambda)$.

4. Thermal Radiation Control by a Microcavity Array

4.1. Fabrication by Nanoimprint

To build a microcavity lamp, we fabricated microcavity array structures on a refractory metal substrate, cut it into filament strips then inserted them into incandescent light bulbs. In the nanofabrication process, we used a nanoimprint method to fabricate microcavity array patterns looking forward to a mass-production process. The details of the fabrication process are shown in Appendix A.

Figure 4a shows a photograph of a 20 × 20 mm polished tantalum (Ta) substrate with a thickness of 100 μm, on which microcavity structures are formed. The structures were fabricated on a single side or both sides of the substrate. Figure 4b shows a scanning ion microscope (SIM) image of the structures. The pattern sizes of the mold are width a = 300 nm, depth d = ~200 nm, and period P = 600 nm. From Figure 4b it is confirmed that a 350-nm-squared cuboidal microcavity with P = 600 nm formed on the substrate. The depth of the cavity is estimated to be ~280 nm by the slanted angle of the SIM image at 30°. The measured depth is shallower than the designed depth of 500 nm. This is because the depth is limited by the differences in the dry etching rate between the Cr mask and the Ta substrate. After fabricating the pattern, the substrate was cut into strips (length: 20 mm, width: 500 μm) using a dicing saw. A single strip was placed into two holding stems to form a filament by welding into a bulb made of Pyrex glass (borosilicate glass). Inert gases (75% Ar and 25% N_2) were put into the bulb. As a result,

we prepared two types of light bulbs with a structure on both sides and a single side. We also prepared a light bulb with a flat filament for reference.

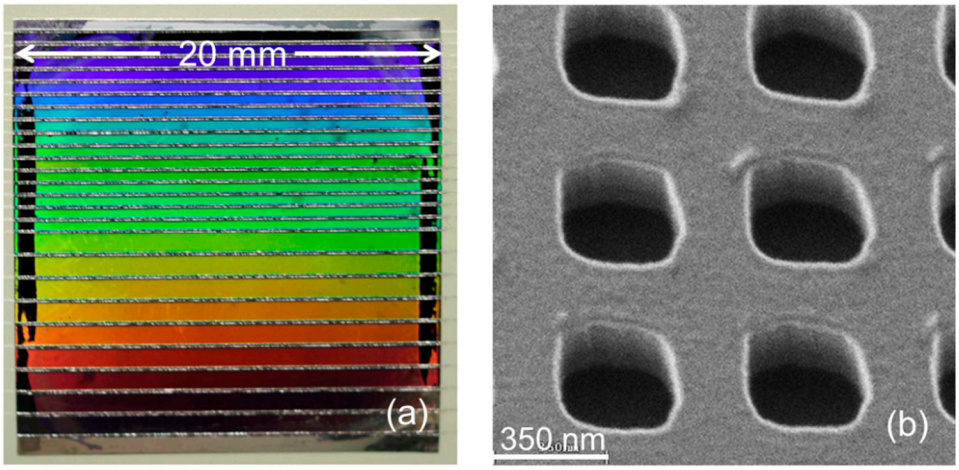

Figure 4. Microcavity filament: (**a**) 20-mm-squared Ta substrate and its split into strips using a dicing-saw process and (**b**) scanning ion microscope (SIM) image of the microcavity. The horizontal scale bar is 350 nm.

Figure 5a shows a photograph of a microcavity lamp prototype. The fact that rainbow colors are seen on the filament shows that periodic structures are formed successfully on the filament. As shown in Figure 5b, the light bulb was set into an E26 socket, and it emitted visible light from the filament by connecting an electric power supply.

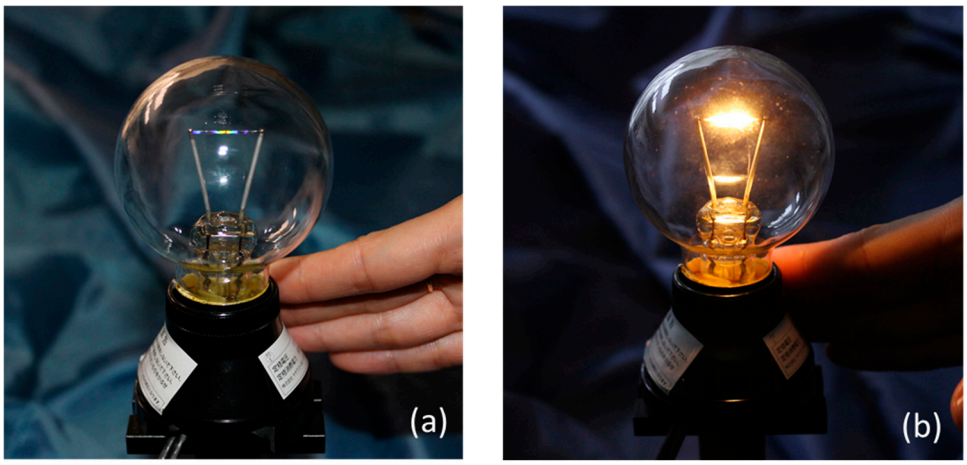

Figure 5. A prototype of the microcavity lamp: (**a**) turning off and (**b**) on.

4.2. Measurements

Measurements of thermal radiation spectra were performed using an integrating sphere for collecting the total luminous flux. A light bulb with a microcavity filament was set into the integrating sphere (LMS-200, Labsphere, Inc., North Sutton, NH, USA) with a diameter of 25 cm. The radiation spectra were measured using a fiber multichannel spectrometer (QE65Pro, Ocean Optics, Inc., Largo, FL, USA) over the wavelength range of 500–1100 nm. A voltage source was used to heat the filament under a constant DC voltage of 1.5 V, where the two-terminal resistance of the light bulb was ~0.1 Ω at room temperature. Next, the light bulb with a flat filament (without a microcavity) was measured under the same conditions as the reference. All measurements were done under a constant electric power of 7.9 W.

We note that the conditions for measuring thermal radiation spectra should be identical for all samples. Two measurement conditions are standard: (i) constant temperature mode and (ii) constant power mode. In constant temperature mode, the radiation spectra are measured, maintaining the same filament temperature for all samples. In constant power mode, radiation spectra are measured maintaining constant electric power to heat a filament. Since it is difficult to directly measure the temperature of a filament inside a light bulb, we used constant power mode here.

4.3. Results and Discussion

Figure 6 shows the results of the thermal radiation spectra of the total flux from two light bulbs: a light bulb with a two-sided microcavity filament ($\Phi_c(\lambda)$) and one with a flat filament ($\Phi_F(\lambda)$) [33]. We can clearly see that the total flux of the microcavity filament is higher than the flat filament. This suggests that the emissivity of the microcavity filament increases compared with the flat filament because the temperature of both filaments was almost identical due to the use of the same input power.

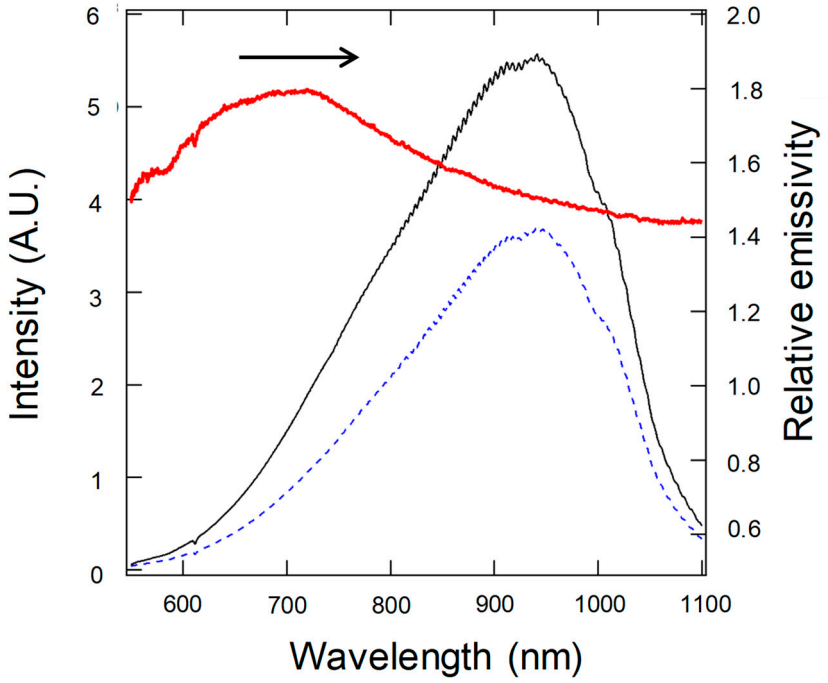

Figure 6. Thermal radiation spectra of the total flux from a microcavity surface (solid line) and flat surface (dotted line). The ratio of total flux (solid red line) is also plotted, representing the enhancement factor.

To analyze the enhancement mechanism, we plotted the enhancement factor defined as $\Phi_c(\lambda)/\Phi_f(\lambda)$, as shown in Figure 6. In the enhancement factor plot, we observe a single broad peak at ~700 nm. The enhancement factor physically means relative spectral emissivity, which is defined as the ratio of the spectral emissivity of a microcavity surface to that of a flat surface: i.e., $\varepsilon_c(\lambda)/\varepsilon_f(\lambda)$, where $\varepsilon_c(\lambda)$ and $\varepsilon_f(\lambda)$ are spectral emissivities at λ of the microcavity and the flat surface, respectively.

4.4. Simulated Results

To analyze the enhancement effect quantitatively, we performed numerical calculations on the spectral absorptivity for the microcavity filament versus the depth of the cavity using a commercially available numerical simulator and the rigorous coupled-wave analysis (RCWA) method (Diffract Mod, RSoft Inc.).

Figure 7a shows the spectral map, $\alpha(\lambda,d)$, of the calculated absorptivity versus the depth, d, of the cavity. We see that $\alpha(\lambda,d)$ has a peak at ~600–900 nm with an α value of 0.9, which then decreases to

~0.1 at $\lambda > 1.0$ μm. These peaks in absorptivity are attributed to the resonant modes inside a single microcavity, and the rapid decrease is due to the cut-off effect in the cavity. However, no peak structure is observed in the measured spectrum, $\Phi_c(\lambda)$, as shown in Figure 6.

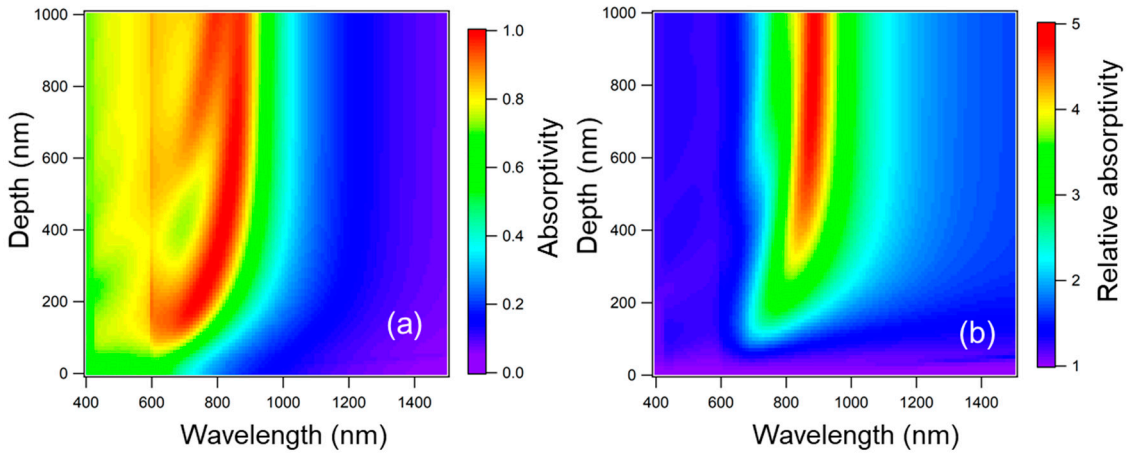

Figure 7. Simulated spectral maps: (**a**) spectral absorptivity/emissivity of a Ta microcavity metasurface to the depth of a microcavity with w = 350 nm and P = 600 nm and (**b**) relative spectral absorptivity/emissivity for the flat surface of Ta.

To compare the simulation to the experimental results, we calculated the relative spectral absorptivity, which is equal to the relative spectral emissivity, $\varepsilon_c(\lambda)/\varepsilon_f(\lambda)$, from Kirchhoff's law. By taking the ratio of absorptivity to the flat surface, we obtain the relative spectral absorptivity/emissivity map $\alpha(\lambda,d)/\alpha(\lambda,0)$ shown in Figure 7b. Note that even a flat Ta surface has moderate broad absorption of α = ~0.5 at $\lambda < 0.6$ μm. We see that absorption enhancement occurs at ~800 nm, and the relative absorptivity increases as the cavity depth increases, as shown in Figure 7b. At a sample depth of d = 280 nm in Figure 4b, the peak position for the relative emissivity is at ~700–900 nm (Figure 7b). This is consistent with the peak position of the experiment in Figure 6. Thus, the broad peak observed for the relative emissivity is attributed to the microcavity effect.

If we can fabricate a sufficiently deep microcavity with $d > 500$ nm, we expect that the thermal radiation spectrum will have a narrower resonant peak at ~850 nm and its relative absorptivity will increase to five, as seen in Figure 7b. However, increasing the cavity depth further is difficult due to the limit of the dry etching process using refractory metals. As a Ta substrate is a hard material compared with Si, the etching contrast ratio between the resist mask and the Ta substrate is not sufficient for deeper etching (see Appendix A). Besides, it is challenging to control the absorptivity in the visible range because typical refractory metals such as Ta, Mo, and W are "dielectric" from the negative value of the dielectric, resulting in absorption in the visible spectrum (see Appendix B) [41]. Actually, even a flat Ta surface (d = 0) has an absorption of α = ~0.5 at λ = 0.4–0.7 μm, as shown in Figure 7a. This means that these metals are far from perfect conductors in the visible range. Hence, a new kind of metasurface is needed beyond the performance of a microcavity array to enhance further the emissivity in the visible spectrum. Plasmonic materials and its metasurfaces are needed beyond conventional refractory metals to control the thermal radiation spectra in the visible range.

5. Thermal Radiation Control by a Refractory Plasmonic Metasurface

5.1. Thermal Radiation Control by Plasmonic Cavities

As described in Section 4, we achieved thermal radiation control using a microcavity filament in the visible range. As a next step, we propose a new kind of filament using a plasmonic metasurface, as illustrated in Figure 8. Figure 8 shows the concept of a plasmonic metasurface where thick microcavities on the refractory metal are replaced by very thin MDM plasmonic cavities. A plasmonic

resonator is very thin (<<λ) compared with the wavelength while a microcavity needs a deep trench structure on the order of the controlled optical wavelength (~λ). Since the thickness of the metasurface is much smaller than the wavelength, the heat capacity is small and is compatible with a planar fabrication process. However, the melting point of conventional plasmonic metals such as Ag and Au are not high enough for thermal radiation control in the visible spectrum.

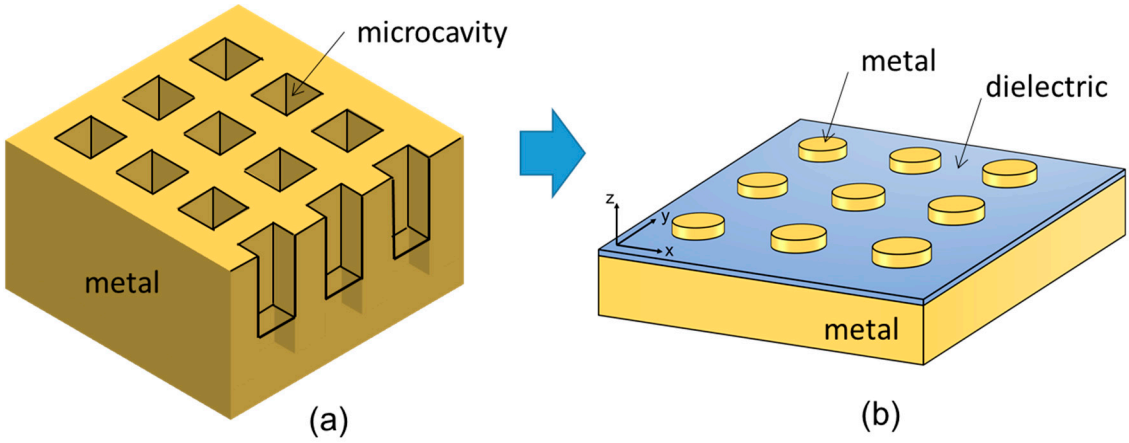

Figure 8. Refractory metasurface (**a**) from a microcavity array to (**b**) a plasmonic cavity array.

In recent years, nitride ceramics such as titanium nitride (TiN) have been proposed and studied as new plasmonic materials operating at higher temperatures (T > 1500 K [42–45]). Melting points of typical plasmonic materials and nitride ceramics are summarized in Table 1. The melting points of these materials are similar to conventional refractory metals, and the permittivity of these materials is negative in the visible range. Hence, those are called "refractory plasmonic materials."

Table 1. Refractory metals and refractory plasmonic materials in order of its melting point.

Material	Melting Point (K)	Permittivity in Visible Range
Ag	1235	ND
Au	1337	ND
SiO_2	1983	D
Mo	2896	D
HfO_2	3031	D
TiN	3203	ND
Ta	3290	D/ND
HfN	3607	ND
W	3695	D

ND: Negative Dielectric; D: Dielectric.

In this study, we used hafnium nitride (HfN) since the melting point of HfN is higher than that of TiN and it is the same order as W. The most crucial property of nitride ceramics is that its permittivity is negative in the visible range like the noble metals. Such a feature is useful for plasmonic materials. The spectral permittivity of conventional and plasmonic refractory metals are shown in Appendix C. If we realize plasmonic metasurfaces using plasmonic refractory materials instead of noble metals, we can control the thermal radiation spectra more precisely and obtain higher Q-value of the plasmonic cavity than that of the microcavity.

Figure 9 shows a schematic of a cross-sectional view of a refractory MDM metasurface, where the Fabry–Pérot (FP) plasmonic resonator disk type based on HfN are arranged in a periodic array. The diameter d, the period P of the resonator, the gap thickness in the dielectric layer, T_g, and the top metal layer (HfN) T_d are shown in Figure 9. We note that the dielectric layer should be selected in accordance with the operating temperature T as such that HfO_2 for T > 2000 K or SiO_2 for T < 2000 K.

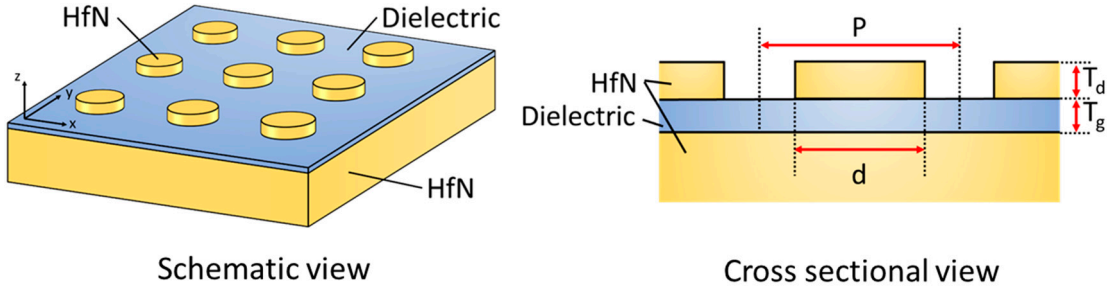

Figure 9. A schematic and cross-sectional view of a metal-dielectric-metal (MDM) metasurface based on hafnium nitride (HfN).

To confirm the efficiency of thermal radiation control by this refractory plasmonic metasurface, we calculated the theoretical radiation spectrum of the MDM metasurface and compared it to a blackbody surface under the condition that both radiation powers are identical, i.e., a constant power mode as described in Section 4.2. Figure 10 shows the simulated results for the thermal radiation spectrum obtained from the metasurface composed of HfN and HfO_2 at T = 2500 K (red line) with d = 40 nm, P = 80 nm, T_g = 60 nm, and T_d = 20 nm. Here, we observe that the highest power radiated from the metasurface is focused on the resonant peak at ~700 nm with a full-width half-maximum (FWHM) value of 571 nm due to the plasmonic resonance in an FP resonator disk. From Figure 10, the equivalent power from the metasurface at T = 2500 K corresponds to the power from a blackbody at T = 1777 K. This means that radiated power from the metasurface at T = 2500 K equals that from the blackbody at only T = 1777 K. According to the Stefan–Boltzmann law, the efficiency is improved by a factor of $(2500/1700)^4 = 3.9$; i.e., the metasurface is 3.9 times more efficient than the blackbody from the viewpoint of power consumption. Additionally, from Figure 10, the radiation intensity at the plasmonic resonant wavelength is more than 10 times greater than that of the blackbody at T = 1777 K.

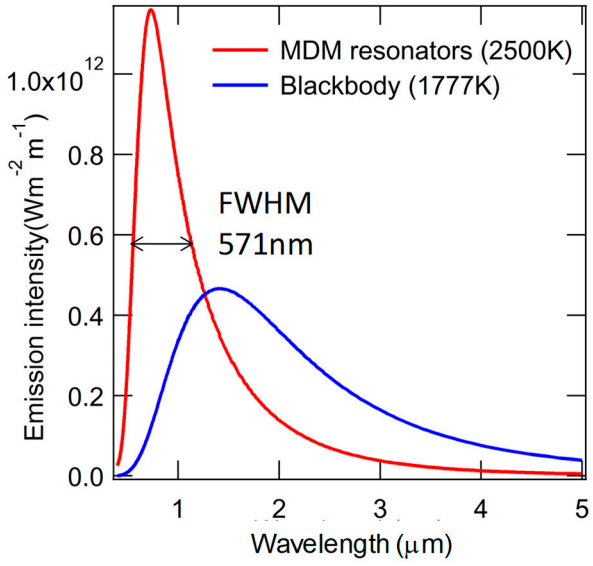

Figure 10. Simulated thermal radiation spectra in constant power mode: radiation spectra from the MDM metasurface (red line) composed of HfN and HfO_2 at T = 2500 K with d = 40 nm, P = 80 nm, T_g = 60 nm, T_d = 20 nm, and the reference blackbody (blue line) at T = 1777 K.

5.2. Fabrication

To demonstrate the thermal radiation control by a refractory plasmonic metasurface, we fabricated MDM metasurfaces based on HfN. In this study, we designed the metasurface to be a perfect absorber in the mid-IR range (~4 μm) instead of in the visible as the first step towards the fabrication of a

"plasmonic" thermal radiation light source. To design and optimize the size parameters for a perfect absorber operating at ~4 μm, we performed numerical simulations using the commercially available finite-difference time-domain method (FDTD) software (Lumerical Inc., Vancouver, BC, Canada) for the metasurface composed of HfN and SiO_2 as shown in Appendix F. From Figure A6, the designed value of diameter d = 1.2 μm was determined for achieving the absorption peak of 4 μm.

Figure 11 shows the MDM metasurface sample with d = 1.14 μm, P = 2.0 μm, T_g = 130 nm, and T_d = 200 nm. The metasurface was fabricated on a 15 × 15 mm square quartz substrate using RF sputtering and electron beam (EB) lithography. The details of the fabrication process are described in Appendix D. The SEM image of meta-atoms is shown in Figure 11c. Additionally, we fabricated a blackbody reference sample by spraying a blackbody spray (TA410KS, Ichinen TASCO Co., Ltd., Osaka, Japan) to the 15 × 15 mm square quartz substrate, as shown in Figure 11a. This blackbody reference has an average absorptivity of α ~0.989 at λ = 3–10 μm.

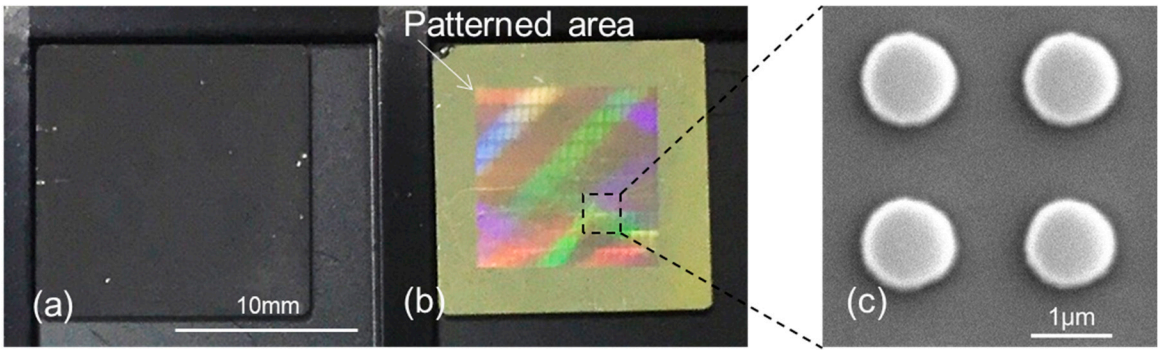

Figure 11. Refractory MDM metasurface and blackbody reference: (**a**) a photograph of the blackbody reference sample, (**b**) the MDM metasurface sample composed of HfN and SiO_2 on a quartz substrate with d = 1.14 μm, P = 2.0 μm, T_g = 130 nm, and T_d = 200 nm. The patterned area is 10 × 10 mm, and (**c**) SEM image of plasmonic resonators.

5.3. Measurements

Before we measured the thermal radiation, we measured the spectral reflectivity $R(\lambda)$ of the metasurface at λ = 3–12 μm using a confocal infrared microscope (HYPERION2000, Bruker Inc., Billerica, MA, USA) and a Fourier transform infrared (FTIR) spectrometer (VERTEX 70v, Bruker Inc., Billerica, MA, USA) at room temperature. IR light partially shielded by slits was focused on a sample through an ×15 (NA: 0.4) Schwarzschild objective lens. The reflected light from the sample was corrected through the objective using a detector and converted through a Fourier transform to calculate reflectivity. Spectral absorptivity, $A(\lambda)$, can be calculated by $A(\lambda) = 1 - R(\lambda)$ if the sample is opaque.

The thermal radiation spectra were measured using an FTIR spectrometer (FT/IR 6000, JASCO Co., Tokyo, Japan) at λ = 3–12 μm. The setup of the thermal radiation measurement is shown in Appendix E. To avoid oxidation of the surface, the sample was set in a vacuum chamber connected to the FTIR spectrometer and heated on a ceramic heater. A DC power supply was used to control the temperature. The temperature was measured by a thermocouple placed on the surface of the sample. The radiation spectra were measured for both the metasurface and the blackbody sample at 573 K. Hence, all measurements were done under the constant temperature of 573 K.

5.4. Results and Discussion

The measured absorptivity spectrum of the MDM metasurface at room temperature is shown in Figure 12a. We observed a single resonant peak at 4.11 μm. To identify the physical origin of the peak, we calculated the spectral absorptivity (see the dashed line in Figure 12a) and field distribution by the FDTD method. The measured spectrum is in good agreement with the simulated spectrum. Figure 12b shows a cross-sectional view of the spatial distribution of the electric field normal to the

incident electric field at 4.11 μm around a meta-atom (plasmonic cavity). Here, we can confirm that the gap plasmon is excited to an FP resonant mode between two metal layers. Hence, the peak in absorptivity around 4 μm is attributed to the plasmonic resonance inside a single plasmonic cavity. Note that the resonant peak position is robust against incident angle for both p- and s-polarizations as shown in Appendix G. The measured FWHM of the peak (~2 μm) is higher than the simulated value (~1.5 μm) while the peak position and the peak value are red-shifted slightly and decreased, respectively. The difference in the FWHM is attributed to the unexpected loss increase in the real materials. The difference in the peak value is probably due to the off-axial arrangement of the incident light through the Schwarzschild objective lens of the infrared microscope. From this measurement, we were able to confirm that the sample was correctly fabricated and operating as designed for a perfect absorber.

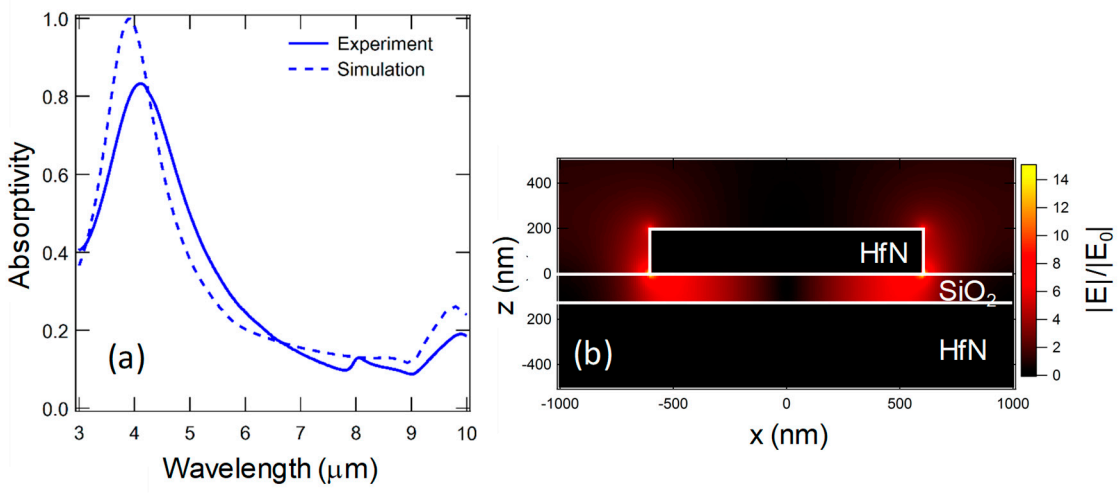

Figure 12. Absorptivity spectra and electric field distribution of the MDM metasurface composed of HfN and SiO_2 with P = 2.0 μm, d = 1.14 μm, T_g = 130 nm, and T_d = 200 nm: (**a**) measured (solid line) and simulated (dashed line) absorptivity spectra at room temperature, and (**b**) normalized electric field distribution around the meta-atom for the resonance at 4.11 μm.

Next, we performed a thermal radiation experiment. Figure 13a shows the thermal radiation spectra at 573 K for the MDM metasurface and reference blackbody sample. We observe that the radiation intensity is suppressed at $\lambda > 5$ μm compared with the blackbody level. Such suppression is caused by the lower absorptivity (emissivity) at $\lambda > 5$ μm, as seen in Figure 12a. Additionally, we can derive the spectral emissivity, ε (λ), of the metasurface from Figure 13a. From Kirchhoff's law, this must be equal to α (λ) shown in Figure 12a if the temperature of a sample is identical. Figure 13b shows the measured spectral emissivity at 573 K of the MDM metasurface. The resonant peak value of ε = ~1 at 4.1 μm with FWHM of ~3 μm is obtained from Figure 13a. This is consistent with the simulated results for absorptivity in Figure 12a (see also the solid line in Figure 13b). These results suggest that perfect absorption/emission occurred as designed, and the cavity loss was increased due to the temperature increase. The FWHM of the measured peak actually is broader than the calculated result of ~1.5 μm. This is evidence of the loss increase caused by the thermal effect.

Finally, we note that the measured radiation spectrum in Figure 13a is not an intrinsic radiation spectrum, but it includes the transmission function of the optical system in the spectrometer (see Appendix E). Hence, it is necessary to separate it out so we can estimate the intrinsic radiation spectrum from the sample. Since we obtained ε (λ), as shown in Figure 13b, we can determine the intrinsic radiation spectrum of the sample by calculating the product of ε (λ) and Planck's law (Equation (1)). Figure 14 shows the presumed spectrum of the intrinsic radiation as well as the blackbody radiation at 573 K. It is clearly observed that thermal radiation from the metasurface is significantly suppressed at longer wavelength region at $\lambda > 5$ μm while the surface temperature of the sample is 573 K. Here, we

point out a crucial fact that the area under the spectral curve of the metasurface is much smaller than that of the blackbody. This indicates that the radiative power from the metasurface is significantly suppressed compared with the blackbody resulting in the achievement of an efficient IR emitter, i.e., we are able to heat a sample quite efficiently by a small amount of power. Such behavior is typical for constant-temperature-mode measurements, which is different from the constant power mode.

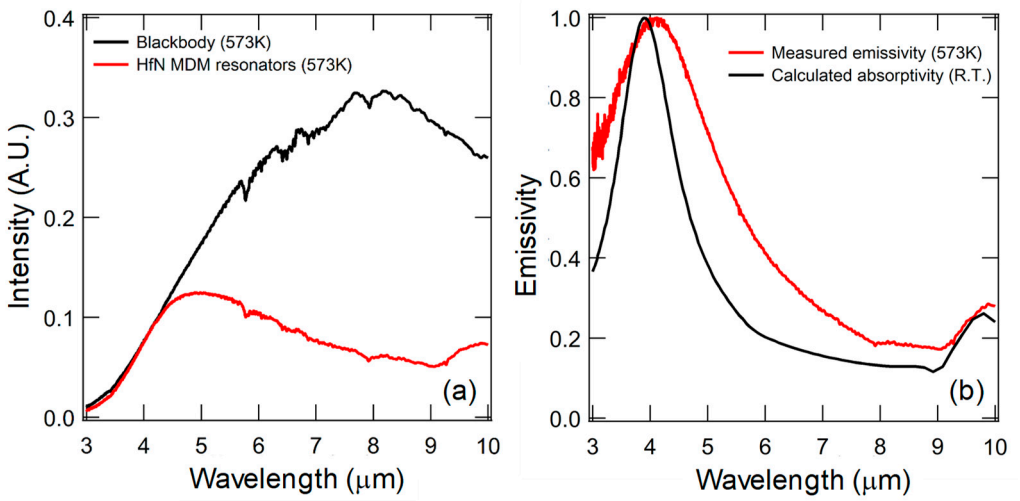

Figure 13. Experimental thermal radiation spectra for the MDM metasurface: (**a**) thermal radiation spectra for the MDM metasurface (red line) and blackbody reference sample (solid line) at 573 K. (**b**) Experimental spectral emissivity at 573 K (red line) derived from (**a**) and simulated absorptivity at room temperature (solid line).

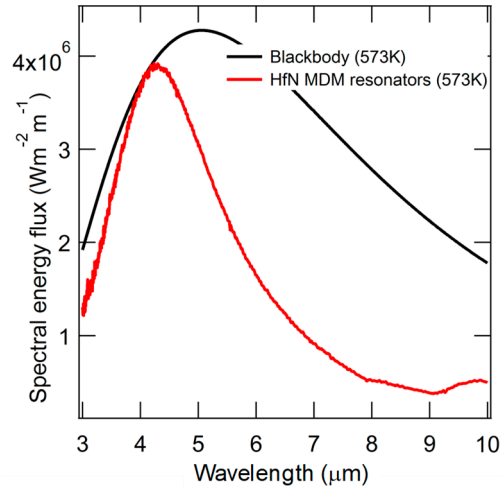

Figure 14. Calculated thermal radiation spectra at 573 K: The radiation spectrum from the MDM metasurface (red line) is calculated from the measured emissivity shown in Figure 13b. The theoretical blackbody radiation spectrum (Equation (1)) at 573 K (solid line) is plotted for reference.

6. Conclusions

We fabricated a prototype of microcavity lamp by a nanoimprint method that is suitable for mass production and demonstrated to control visible-light spectrum using a refractory metasurface made of Ta with an optical microcavity implemented into an incandescent light bulb. It was confirmed that thermal radiation intensity from the microcavity filament was increased 1.8 times compared to the flat filament under the constant power input. Then, we fabricated and demonstrated the thermal radiation control in mid-IR range by using an MDM plasmonic metasurface composed of a refractory plasmonic cavity made of HfN. A single narrow resonant peak was observed at designed wavelength

as well as the suppression of thermal radiation in wide mid-IR range under the condition of constant surface temperature.

We revaluated a thermal radiation light source as an efficient light source from the perspective of energy conversion. For a future energy-saving society, it is vital to reconsider thermal radiation sources as energy-saving technology.

Author Contributions: J.T. conceived the idea of incandescent light bulbs based on refractory metasurface. H.T. and A.K. performed the numerical simulations. H.T. and K.K. performed the experiments. J.T. analyzed the experimental data and wrote the initial draft of the manuscript. J.T. supervised the project. All the authors discussed the results and contributed to the writing of the manuscript.

Funding: This research was funded in part by the Photonics Advanced Research Center (PARC) from the Ministry of Education, Culture, Sports, Science and Technology, Japan (MEXT) and the JSPS Core-to-Core Program, and A. Advanced Research Networks (Advanced Nanophotonics in the Emerging Fields of Nano-imaging, Spectroscopy, Nonlinear Optics, Plasmonics/Metamaterials, and Devices).

Acknowledgments: We would like to thank Yosuke Ueba and Yusuke Nagasaki for useful discussions. A part of this work was supported by the "Nanotechnology Platform Project (Nanotechnology Open Facilities in Osaka University)" of the Ministry of Education, Culture, Sports, Science, and Technology, Japan [No.: F-17-OS-0011, S-17-OS-0011].

Conflicts of Interest: The authors declare no conflicts of interest. The funders had no role in the design of the study, in the collection, analyses, or interpretation of data; in the writing of the manuscript, or in the decision to publish the results.

Appendix A

The microcavity filaments were fabricated by a nanoimprint process suitable for mass production as described below. Figure A1 shows the fabrication process of a microcavity array onto a Ta substrate. At first, a 3-inch Si wafer (thickness 380 μm) was prepared, and the electron beam (EB) resist (ZEP520A-7) spin-coated to a thickness of 300 nm using a spinner for 60 s at 4000 rpm. It was then baked for 5 min at 180 °C. After that, a 20 × 20 mm square microcavity array pattern was drawn onto the EB resist using a 50-kV electron beam (EB) lithography system (F5112+VD01; ADVANTEST Co., Tokyo, Japan). After developing the resist, the Si wafer was dry-etched by an inductively coupled plasma (ICP) etching machine (EIS-700, ELIONIX Inc., Tokyo, Japan) to transfer the pattern to the substrate, resulting in a Si master mold with 300 × 300 nm square holes, 300 nm wall width, and approximately 200 nm depth. Then, the master mold was duplicated onto a photocrosslinkable resin film under heat and high-pressure conditions, resulting in an intermediate resin membrane (IRM). These IRMs are used for mass production in the future so the master mold can be preserved.

Next, we prepared polished Ta substrates (20 × 20 mm squares with a thickness of 100 μm) for making filaments. A 30-nm-thickness Cr layer was deposited on the Ta substrate, and a photoresist (MUR-XR2-150, Maruzen Petrochemical Co., Ltd., Tokyo, Japan) was spin-coated on the substrate to a thickness of 215 nm by using a spinner at 3000 rpm. Then, the sample was placed in a vacuum chamber, and the IRM placed on a quartz cylinder was pressed onto the resist under UV light irradiation, resulting in stamping the pattern onto the resist residing on the substrate with the Cr layer. Since the IRM and the cylinder are transparent, it can be used as a template to transfer a pattern to a photoresist under UV irradiation.

After removing the IRM, the Ta substrate was dry-etched through the resist and the Cr mask film using an electron cyclotron resonance (ECR) ion shower machine (EIS-200ER, ELIONIX Inc., Tokyo, Japan) and ICP etching machine (EIS-700, ELIONIX Inc., Tokyo, Japan). The etching depths are 3.2 nm for the Cr layer and 18 nm for the Ta substrate. Finally, the resist pattern was transferred to the Ta substrate, as shown in Figure 4b. The resulting cavity size was wider than the mold (350 × 350 nm square holes, 250-nm wall width, and ~280-nm depth). Note that such a widening effect was caused by the dry-etching process and was calibrated by designing the EB lithography process.

We fabricated three kinds of Ta substrate: (i) the microcavity on a single side, (ii) the microcavity on both sides, and (iii) a plane without patterning for reference. In the case of (i), we performed the

process once. For (ii), we repeated the process twice. Finally, the Ta substrates were cut into narrow 500-μm strips as shown in Figure 4a.

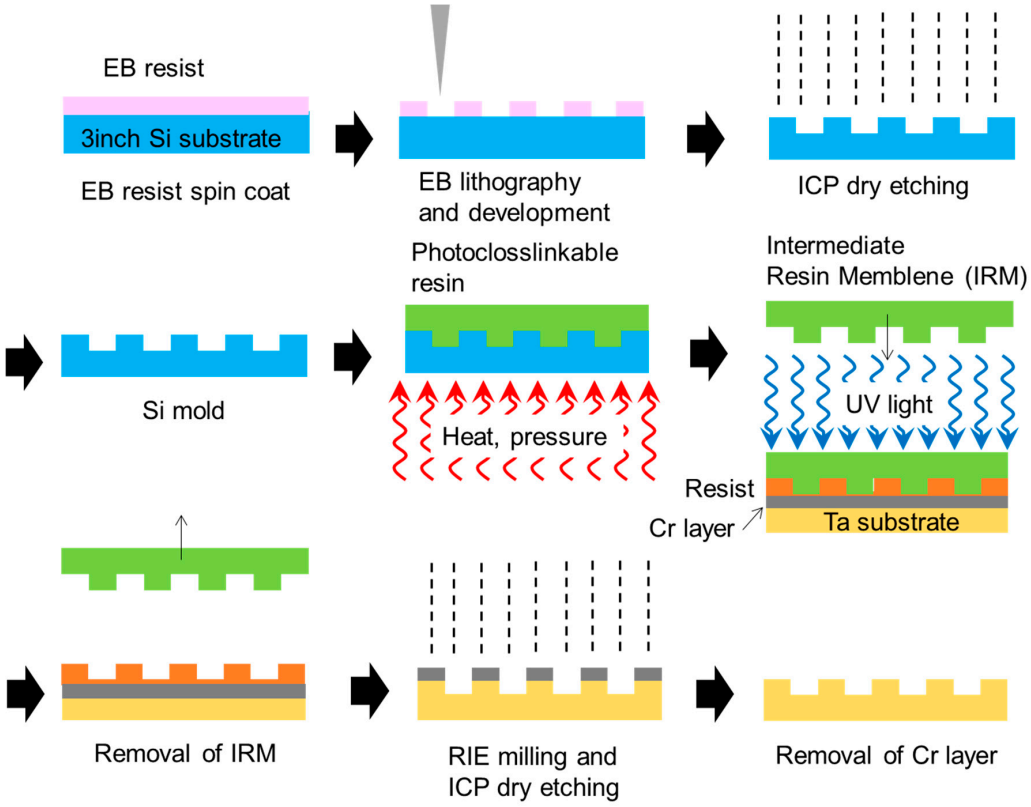

Figure A1. Nanoimprint process for fabricating microcavity filaments.

Appendix B

Figure A2 shows the relative permittivity spectra of conventional refractory metals (W, Ta, and Mo) [41]. The real part of the permittivity for W and Mo are both positive in the visible range ($\lambda < 0.8$ μm). The real part of the permittivity of Ta switches from negative to positive below 0.6 μm. The imaginary part of the permittivity of Ta is ~1/2 that of W and Mo.

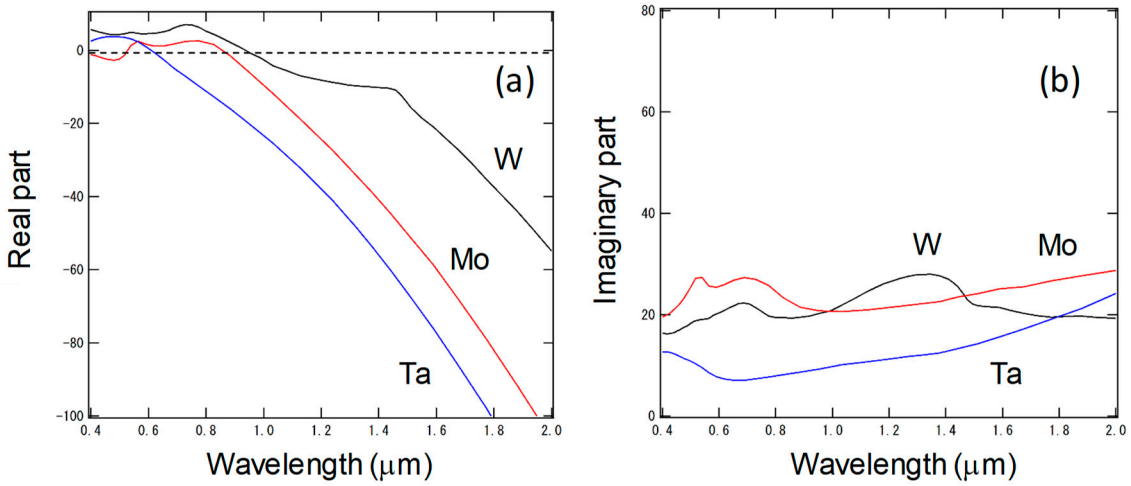

Figure A2. Spectral relative permittivities of conventional refractory metals (W, Ta, and Mo): (**a**) real and (**b**) imaginary part of the relative permittivity [41].

Appendix C

Figure A3 shows the relative permittivity spectra of conventional plasmonic metals (Au, Ag, and Al) [41], and refractory plasmonic materials (TiN and HfN) [43]. The real part of the permittivity of HfN is negative within the entire visible range and is very close to that of Au at $\lambda < 0.6$ μm. The imaginary part of the permittivity of HfN is ~1/2 that of TiN in the visible range.

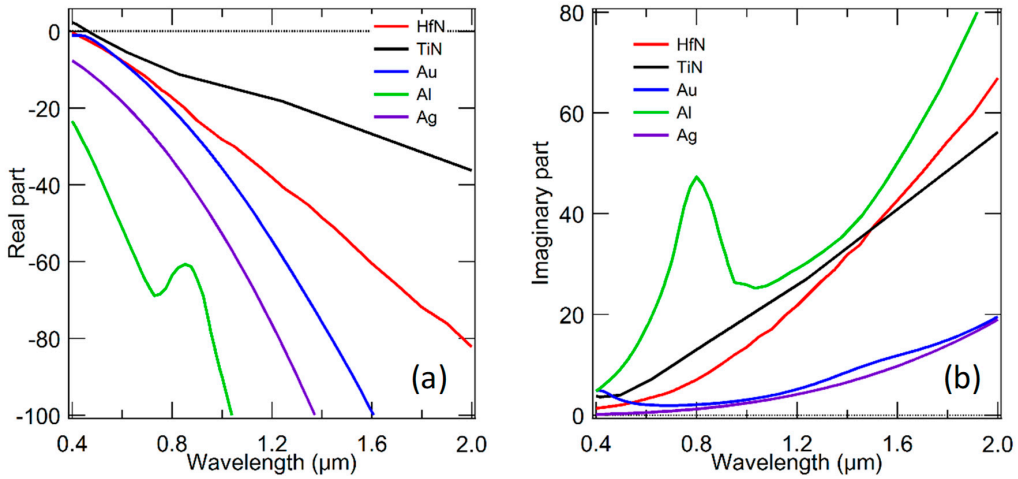

Figure A3. Spectral relative permittivity of conventional plasmonic metals (Au, Ag, and Al) [41] and refractory plasmonic materials (TiN and HfN) [43]: (**a**) real and (**b**) imaginary part of the relative permittivities.

Appendix D

Figure A4 shows the fabrication process for the refractory MDM metasurface. First, a HfN layer and a 130-nm-thick SiO_2 layer were deposited on a quartz substrate (15 × 15 mm) using an RF sputtering system (SVC-700LRF, SANYU Electron, Tokyo, Japan). In fabricating the HfN layer, we used an HfN target (Toshima Manufacturing Co., Ltd., Saitama, Japan) under an Ar gas flow rate of 25 sccm at 2×10^{-4} Pa. Next, hexamethyldisilazane (HMDS) was spin-coated using a spinner for 90 s at 5000 rpm. Then, a photoresist (TSMR-8900) was spin-coated to a thickness of 700 nm using a spinner for 90 s at 5000 rpm. The metasurface patterns were exposed using a mask-less UV lithography system (DL-1000, Nanosystem Solutions Inc., Tokyo, Japan) then developed. Next, a 200-nm-thick HfN layer was deposited by RF sputtering. Finally, the HfN layer was lifted off using N-methyl-2-pyrrolidone (NMP).

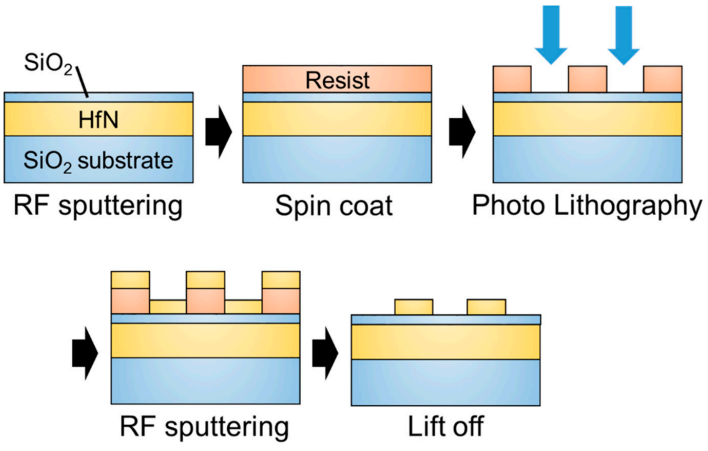

Figure A4. Fabricating the refractory MDM metasurface.

Appendix E

Figure A5 shows the experimental setup for measuring the thermal radiation spectrum. The optical system was placed in a vacuum chamber connected to an FTIR spectrometer (FT/IR 6000, JASCO Co., Tokyo, Japan) through a tunnel tube. The vacuum chamber and the FTIR were pumped to 2.0×10^2 Pa and 1.4×10^2 Pa, respectively. The spectral resolution was set to 4 cm^{-1}, and a DLATGS detector was used for the measurement. The device is shown in Figure 12 and was placed on a micro-ceramic heater (MS-1000, Sakaguchi E.H VOC Corp., Tokyo, Japan). The temperature of the sample was measured by a K-type sheath thermocouple (T350251H, Sakaguchi E.H VOC Corp., Tokyo, Japan) placed on the surface of the sample. The measurements were performed at 573 K.

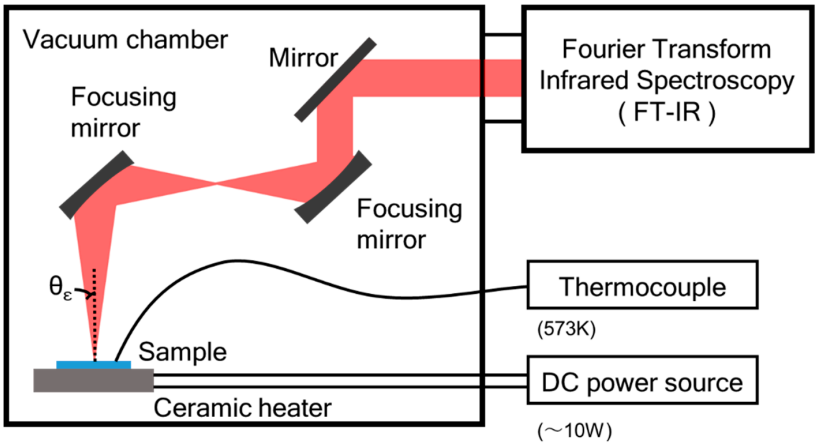

Figure A5. Experimental setup for measuring the thermal radiation spectrum. The sample is set on a ceramic heater in a vacuum chamber that is connected to the FTIR spectrometer through a tunnel tube.

Appendix F

Figure A6 shows simulated spectral absorptivity to the diameter d of an MDM metasurface composed of HfN and SiO_2 (see Figure 9) with P = 2.0 μm, T_g = 130 nm, and T_d = 200 nm. The peak position of absorption caused by gap plasmon mode in the circular cavity can be changed from 3.0 to 7.0 μm by changing d.

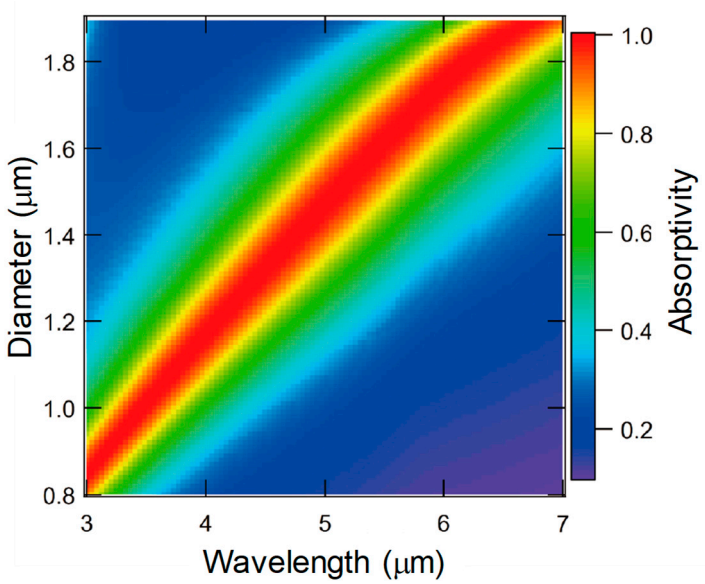

Figure A6. Simulated spectral absorptivity/emissivity map to the diameter of an MDM metasurface composed of HfN and SiO_2 with P = 2.0 μm, T_g = 130 nm, and T_d = 200 nm.

Appendix G

Figure A7 shows simulated spectral absorptivity to the incident angle to an MDM metasurface composed of HfN and SiO_2 (see Figure 9). The single absorption peak caused by gap plasmon mode in the circular cavity is observed at ~4.5 μm for both polarizations, which is not strongly dependent on incident angle. The strong angle-dependent steep absorption is caused by diffraction at 2.5–4.0 μm only for p-polarization as shown in (a). Note that the designed value of d = 1.2 μm is slightly greater than that of the experimental value (d = 1.14 μm).

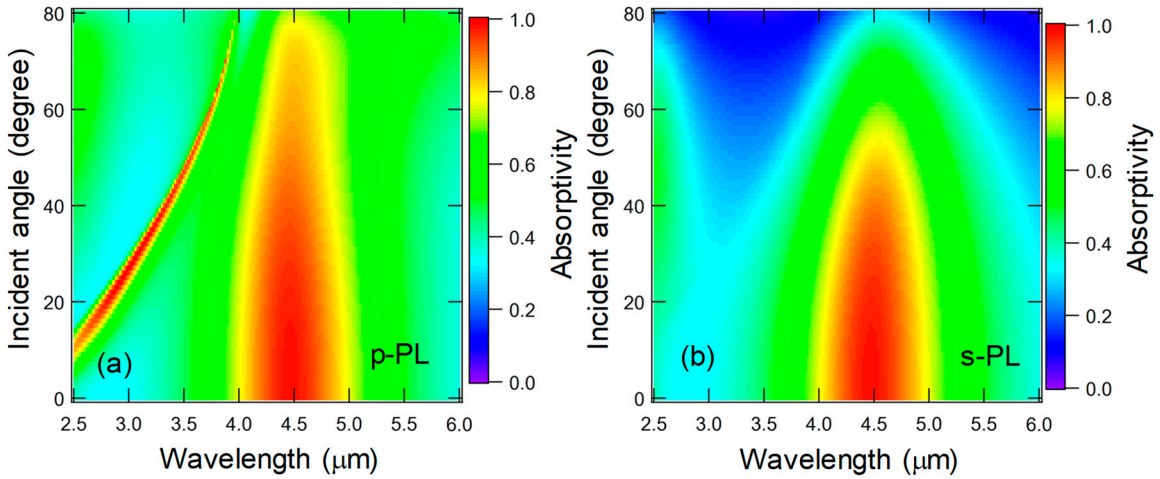

Figure A7. Simulated spectral absorptivity/emissivity maps to the incident angle to an MDM metasurface composed of HfN and SiO_2 with P = 2.0 μm, d = 1.2 μm, T_g = 130 nm, and T_d = 200 nm: (**a**) p-polarization and (**b**) s-polarization.

References

1. Takahara, J.; Ueba, Y.; Nagatsuma, T. Thermal radiation control by microcavity and ecological incandescent lamps. *Jpn. J. Opt.* **2010**, *39*, 482–488.
2. Takahara, J.; Ueba, Y. Thermal Infrared Emitters by Plasmonic Metasurface. *Proc. SPIE* **2013**, *8818*, 88180X.
3. Waymouth, J.F. Where will the next generation of lamps come from? *J. Illum. Energy Inst. Jpn.* **1990**, *74*, 800. [CrossRef]
4. Waymouth, J.F. Optical Light Source Devices. U.S. Patent 5,079,473, 7 January 1992.
5. Hesketh, P.J.; Zemalr, J.N.; Gebhart, B. Organ pipe radiant modes of periodic micromachined silicon surface. *Nature* **1986**, *324*, 549–551. [CrossRef] [PubMed]
6. Maruyama, S.; Kashiwa, T.; Yugami, H.; Esashi, M. Thermal radiation from two-dimensionally confined modes in microcavities. *Appl. Phys. Lett.* **2001**, *79*, 1393–1395. [CrossRef]
7. Kusunoki, F.; Kohama, T.; Hiroshima, T.; Fukumoto, S.; Takahara, J.; Kobayashi, T. Narrow-Band Thermal radiation with Low Directivity by Resonant Modes inside Tungsten Microcavities. *Jpn. J. Appl. Phys.* **2004**, *43*, 5253–5258. [CrossRef]
8. Lin, S.Y.; Fleming, J.G.; Chow, E.; Bur, J.; Choi, K.K.; Goldberg, A. Enhancement and suppression of thermal emission by a three-dimensional photonic crystal. *Phys. Rev.* **2000**, *62*, R2243–R2246. [CrossRef]
9. Zoysa, M.D.; Asano, T.; Mochizuki, K.; Oskooi, A.; Inoue, T.; Noda, S. Conversion of broadband to narrowband thermal emission through energy recycling. *Nat. Photonics* **2012**, *6*, 535–539. [CrossRef]
10. Ikeda, K.; Miyazaki, H.T.; Kasaya, T.; Yamamoto, K.; Inoue, Y.; Fujimura, K.; Kanakugi, T.; Okada, M.; Hatada, K.; Kitagawa, S. Controlled thermal emission of polarized infrared waves from arrayed plasmon nanocavities. *Appl. Phys. Lett.* **2008**, *92*, 021117. [CrossRef]
11. Miyazaki, H.; Ikeda, K.; Kasaya, T.; Yamamoto, K.; Inoue, Y.; Fujimura, K.; Kanakugi, T.; Okada, M.; Hatade, K.; Kitagawa, S. Thermal emission of two-color polarized infrared waves from integrated plasmon cavities. *Appl. Phys. Lett.* **2008**, *92*, 141114. [CrossRef]

12. Schuller, J.A.; Taubner, T.; Brongersma, M.L. Optical antenna thermal emitters. *Nat. Photonics* **2009**, *3*, 658–661. [CrossRef]
13. Greffet, J.J.; Carminati, R.; Joulain, K.; Mulet, J.P.; Mainguy, S.; Chen, Y. Coherent emission of light by thermal sources. *Nature* **2002**, *416*, 61–62. [CrossRef] [PubMed]
14. Kusunoki, F.J.; Kobayashi, T. Qualitative change of resonant peaks in thermal emission from periodic array of microcavities. *Electron. Lett.* **2003**, *39*, 23–24. [CrossRef]
15. Biener, G.; Dahan, N.; Niv, A.; Kleiner, V.; Hasmana, E. Highly coherent thermal emission obtained by plasmonic bandgap structures. *Appl. Phys. Lett.* **2008**, *92*, 081913. [CrossRef]
16. Ueba, Y.; Takahara, J.; Nagatsuma, T. Thermal radiation control in the terahertz region using the spoof surface plasmon mode. *Opt. Lett.* **2011**, *36*, 909–911. [CrossRef]
17. Yang, Z.Y.; Ishii, S.; Yokoyama, T.; Dao, T.D.; Sun, M.-G.; Nagao, T.; Chen, K.-P. Tamm plasmon selective thermal emitters. *Opt. Lett.* **2016**, *41*, 4453–4456. [CrossRef]
18. Landy, N.I.; Sajuyigbe, S.; Mock, J.J.; Smith, D.R.; Padilla, W.J. Perfect Metamaterial Absorber. *Phys. Rev. Lett.* **2008**, *100*, 207402. [CrossRef]
19. Watts, C.M.; Liu, X.; Padilla, W.J. Metamaterial Electromagnetic Wave Absorbers. *Adv. Mater.* **2012**, *24*, OP98. [CrossRef]
20. Lee, B.J.; Wang, L.P.; Zhang, Z.M. Coherent thermal emission by excitation of magnetic polaritons between periodic strips and a metallic film. *Opt. Express* **2008**, *16*, 11328–11336. [CrossRef]
21. Puscau, I.; Schaich, W.L. Narrow-band, tunable infrared emission from arrays of microstrip patches. *Appl. Phys. Lett.* **2008**, *92*, 233102. [CrossRef]
22. Liu, X.; Starr, T.; Starr, A.F.; Padilla, W.J. Infrared Spatial and Frequency Selective Metamaterial with Near-Unity Absorbance. *Phys. Rev. Lett.* **2010**, *104*, 207403. [CrossRef] [PubMed]
23. Liu, X.; Tyler, T.; Starr, T.; Starr, A.F.; Jokerst, N.M.; Padilla, W.J. Taming the Blackbody with Infrared Metamaterials as Selective Thermal Emitters. *Phys. Rev. Lett.* **2011**, *107*, 045901. [CrossRef] [PubMed]
24. Nielsen, M.G.; Pors, A.; Albrektsen, O.; Bozhevolnyi, S.I. Efficient absorption of visible radiation by gap plasmon resonators. *Opt. Express* **2012**, *20*, 13311–13319. [CrossRef] [PubMed]
25. Ueba, Y.; Takahara, J. Spectral control of thermal radiation by metasurface with a sprit-ring resonator. *Appl. Phys. Express* **2012**, *5*, 122001–122003. [CrossRef]
26. Ito, K.; Toshiyoshi, H.; Iizuka, H. Densely-tiled metal-insulator-metal metamaterial resonators with quasi-monochromatic thermal emission. *Opt. Express* **2016**, *24*, 12803–12811. [CrossRef]
27. Yokoyama, T.; Dao, T.D.; Chen, K.; Ishii, S.; Sugavaneshwar, R.P.; Kitajima, M.; Nagao, T. Spectrally Selective Mid-Infrared Thermal Emission from Molybdenum Plasmonic Metamaterial Operated up to 1000 °C. *Adv. Opt. Mat.* **2016**, *4*, 1987. [CrossRef]
28. Miyazaki, H.T.; Kasaya, T.; Iwanaga, M.; Choi, B.; Sugimoto, Y.; Sakoda, K. Dual-band infrared metasurface thermal emitter for CO_2 sensing. *Appl. Phys. Lett.* **2014**, *105*, 121107. [CrossRef]
29. Matsuno, Y.; Sakurai, A. Perfect infrared absorber and emitter based on a large-area metasurface. *Opt. Mat. Express* **2017**, *7*, 618–626. [CrossRef]
30. Ogawa, S.; Kimata, M. Metal-Insulator-Metal-Based Plasmonic Metamaterial Absorbers at Visible and Infrared Wavelengths: A Review. *Materials* **2018**, *11*, 458. [CrossRef]
31. Baranov, D.G.; Xiao, Y.; Nechepurenko, I.A.; Krasnok, A.; Alù, A.; Kats, M.A. Nanophotonic engineering of far-field thermal emitters. *Nat. Mater.* **2019**, *18*, 920–930. [CrossRef]
32. Sai, H.; Kanamori, Y.; Yugami, H. High-temperature resistive surface grating for spectral control of thermal radiation. *Appl. Phys. Lett.* **2003**, *82*, 1685–1687. [CrossRef]
33. Takahara, J. Renaissance of incandescent light bulbs through nanotechnology. *Oyo Buturi* **2015**, *84*, 564–567.
34. Takahara, J.; Kimino, K. Visible Spectral Control of Incandescent Light Bulbs by Microcavity Filament. In Proceedings of the Abstracts of 15th International Symposium on the Science and Technology of Lighting (LS15), Kyoto, Japan, 22–27 May 2016. 23P-LL1.
35. Ilic, O.; Bermel, P.; Chen, G.; Joannopoulos, J.D.; Celanovic, I.; Soljačić, M. Tailoring high-temperature radiation and the resurrection of the incandescent source. *Nat. Nanotech.* **2016**, *11*, 320–324. [CrossRef] [PubMed]
36. Shimogaki, K.; Iwai, I.; Yoshiike, H. The Luminous Efficacy of an Incandescent Lamp Which has an Infrared Reflective Film. *J. Illum. Eng. Inst. Jpn.* **1984**, *68*, 72–76. [CrossRef]

37. The Illuminating Engineering Institute of Japan (IEI-J). *Lighting Handbook (Compact Version)*; Ohmsha: Tokyo, Japan, 2006; Volume 3 2-1-2.
38. IEI-J. *Lighting Databook (New Edition)*; Ohmsha: Tokyo, Japan, 1968; Volume 3-1-2.
39. IEI-J. *Lighting Handbook (Compact Version)*; Ohmsha: Tokyo, Japan, 2006; Volume 3 2-2-2.
40. IEI-J. *34th Textbook of Lighting Basic Course (New Edition)*; IEI-J: Tokyo, Japan, 2013; pp. 2–23.
41. Palik, E.D. *Handbook of Optical Constants of Solids*; Academic Press: San Diego, CA, USA, 1985.
42. Boltasseva, A.; Atwater, H.A. Low-Loss Plasmonic Materials. *Science* **2011**, *331*, 290–291. [CrossRef]
43. Naik, G.V.; Shalaev, V.M.; Boltasseva, A. Alternative Plasmonic Materials: Beyond Gold and Silver. *Adv. Mater.* **2013**, *25*, 3264–3294. [CrossRef]
44. Guler, U.; Boltasseva, A.; Shalaev, V.M. Refractory Plasmonics. *Science* **2014**, *344*, 263–264. [CrossRef]
45. Kumar, M.; Umezawa, N.; Ishii, S.; Nagao, T. Examining the Performance of Refractory Conductive Ceramics as Plasmonic Materials: A Theoretical Approach. *ACS Photonics* **2015**, *3*, 43–50. [CrossRef]